

Mechanism of Action of the Tungsten Dopant in LiNiO₂ Positive Electrode Materials

Chenxi Geng, Divya Rathore, Dylan Heino, Ning Zhang, Ines Hamam, Nafiseh Zaker, Gianluigi A. Botton, Roe Omessi, Nutthaphon Phattharasupakun, Toby Bond, Chongyin Yang,* and J. R. Dahn*

The addition of tungsten has been reported to greatly improve the capacity retention of Ni-rich layered oxide cathode materials in lithium-ion batteries. In this work, Ni(OH)₂ precursors, coated with WO₃ and also W-containing precursors prepared by co-precipitation followed by heat treatment with LiOH·H₂O, are studied. Structural analysis and electron microscopy show that W is incorporated as amorphous Li_xW_yO_z phases concentrated in all the grain boundaries between the primary particles of LiNiO₂ (LNO) and on the surface of the secondary particles. Tungsten does not substitute for Ni or Li in the LNO lattice no matter how W is added at the precursor synthesis stage. Scanning electron microscopy (SEM) images show that adding W greatly suppresses primary particle growth during synthesis. In agreement with previous literature reports, cycling test results show that 1% W added to LNO can greatly improve charge–discharge capacity retention while also delivering a high specific capacity. The Li_xW_yO_z amorphous phases act as coating layer on both the primary and secondary particles, restrict primary particle growth during synthesis and increase the resistance of the secondary particles to microcracking.

sities.^[1–7] However, the practical capacity of many commercial Ni-rich cathodes is still limited to <200 mAh g⁻¹ to guarantee a long cycle life, and the incorporated Co is becoming increasingly problematic in terms of price and sustainability. To overcome these limitations, increasing the fraction of Ni in the materials to increase the capacity and reducing the use of Co is a common strategy. However, materials with a very high Ni content show faster chemo-mechanical degradation such as microcracking of secondary particles during charge discharge cycling.^[8,9] Hence, preparing high-Ni cathodes with satisfactory cycling stability remains challenging.

Many researchers have worked very hard to solve this problem. The addition of tungsten (W) has been reported to be particularly effective to improve the cycling stability of Ni-rich and Li-rich materials.^[10–15] However, the underlying

mechanism for the action of W remains puzzling. For a starter, some researchers claim that the W dopant is located in the TM sites as a substituent, which seems questionable.^[13] W⁶⁺ is the most stable oxidation state of W and is closest in size to Ni³⁺ so one would expect W⁶⁺ to be the oxidation state of W substituted for Ni in LiNiO₂. However, such a substitution

1. Introduction

Ni-rich layered Li transition metal oxides, such as LiNi_xCo_yAl_{1-x-y}O₂ (NCA, $x > 0.8$) and LiNi_xMn_yCo_(1-x-y)O₂ (NMC, $x \geq 0.5$), are the top choices of cathode materials for electric vehicles owing to their superior energy and power den-

C. Geng, J. R. Dahn
Department of Process Engineering and Applied Science
Dalhousie University
Halifax, NS B3H 4R2, Canada
E-mail: jeff.dahn@dal.ca

D. Rathore, N. Zhang, N. Phattharasupakun, T. Bond, C. Yang,
J. R. Dahn
Department of Physics and Atmosphere Science
Dalhousie University
Halifax, NS B3H 4R2, Canada
E-mail: c.yang@dal.ca

D. Heino, I. Hamam, J. R. Dahn
Department of Mechanical Engineering
Dalhousie University
Halifax, NS B3H 4R2, Canada

N. Zaker, G. A. Botton
Materials Science and Engineering
McMaster University
Hamilton, Ontario L8S 4L7, Canada

G. A. Botton, T. Bond
Canadian Light Source
44 Innovation Boulevard, Saskatoon, Saskatchewan S7N 2V3, Canada

R. Omessi
Department of Electrical and Computer Engineering
Dalhousie University
Halifax, NS B3H 4R2, Canada

N. Phattharasupakun
Department of Chemical and Biomolecular Engineering
School of Energy Science and Engineering
Vidyasirimedhi Institute of Science and Technology
Rayong 21210, Thailand

 The ORCID identification number(s) for the author(s) of this article can be found under <https://doi.org/10.1002/aenm.202103067>.

DOI: 10.1002/aenm.202103067

will create numerous defects and structural distortions to balance the charge difference, which is unlikely to be energetically favorable. Therefore, a close examination of the location of W in LiNiO_2 and the corresponding mechanism that is responsible for improving charge–discharge capacity retention is urgently required.

In this work, we investigated the mechanism of action of W in LiNiO_2 (LNO). LNO with different mole ratios of W:(Ni+W) (0.5, 1, 2, and 4 mol%), which are denoted as W0.5-LNO, W1-LNO, W2-LNO, and W4-LNO, were synthesized by coating nanosized WO_3 on $\text{Ni}(\text{OH})_2$ by a dry particle fusion method previously reported by our group, followed by heating with $\text{LiOH}\cdot\text{H}_2\text{O}$. W-containing $\text{Ni}(\text{OH})_2$ precursors were also prepared by coprecipitation and these were subsequently heated with $\text{LiOH}\cdot\text{H}_2\text{O}$. X-ray diffraction (XRD) and electron energy loss spectroscopy (EELS) experiments in a transmission electron microscope (TEM) were used to examine the structure of the materials synthesized in this work and to determine the W distribution inside materials. Electrochemical measurements made with coin cells verified the excellent charge–discharge capacity retention of materials synthesized with 1% W.

2. Results and Discussion

X-ray diffraction patterns were collected from 15° to 70° for the materials heated with $\text{LiOH}\cdot\text{H}_2\text{O}$ and all the materials demonstrated a well-developed layered structure as shown in Figure 1A. The peak-height normalized (003) peak broadened with increasing amounts of W as shown clearly in Figure 1B. It is known that the full width at a half maximum (FWHM) of the XRD peak is inversely proportional to the crystallite grain size,^[16,17] so the peak broadening indicates decreasing crystallite grain size with increasing W content. The (003) peak broad-

ening could also be attributed to the increased micro strain in lattice due to Ni–Li mixing.^[18] More importantly, there was an amorphous hump which appears near the (003) peak and which increases in intensity with increasing amounts of W, while an impurity peak appeared at 24° and also got more intense as the W fraction increased (Figure 1C). The amorphous hump and impurity peak, which do not originate from the layered structure, raised the question whether the added W atoms were incorporated into the layered structure or stayed outside the grains of primary particles as a secondary phase.

Rietveld refinements were performed assuming an $\alpha\text{-NaFeO}_2$ (space group $R\bar{3}m$) hexagonal layered structure in which Li occupies the 3a site, transition metals occupy the 3b site, and oxygen occupies the 6c site. The refinement results are shown in Table S2 in the Supporting Information. There is an increase of Ni atoms in the Li layer ($\%\text{Ni}_{\text{Li}}$) with increasing W fraction, from $\approx 2.5\%$ in LNO to 8.9% in W4-LNO, while the lattice parameters a and c also increase as the W fraction increases. One might argue that W^{6+} gets doped into the transition metal layer, and therefore more Ni^{3+} was reduced to Ni^{2+} to maintain charge neutrality. Ni^{2+} has a similar ionic radius ($r_{\text{Ni}^{2+}} = 0.69 \text{ \AA}$, $r_{\text{Ni}^{3+}} = 0.56 \text{ \AA}$) to Li^+ ($r_{\text{Li}^+} = 0.76 \text{ \AA}$),^[19] which facilitates Ni and Li mixing and results in the higher $\%\text{Ni}_{\text{Li}}$ with higher fraction of W.^[13] However, our DFT calculation^[20] show that it is not preferable for W to be incorporated in the layered phase lattice. Instead, we believe that W is incorporated in $\text{Li}_x\text{W}_y\text{O}_z$ ($x/y > 1$) phases in the grain boundaries between primary particles, which takes more Li from LiNiO_2 making it lithium deficient and thus having a higher $\%\text{Ni}_{\text{Li}}$ and increased lattice constants.

In order to further investigate the amorphous hump and impurity peak, we made W4-LNO with extra Li added, which corresponds to $\text{Li}/(\text{Ni}+\text{W}) = 1.06$ (our normal W4-LNO sample has a $\text{Li}/(\text{Ni}+\text{W})$ ratio of 1.02). W4-LNO also had a well-developed

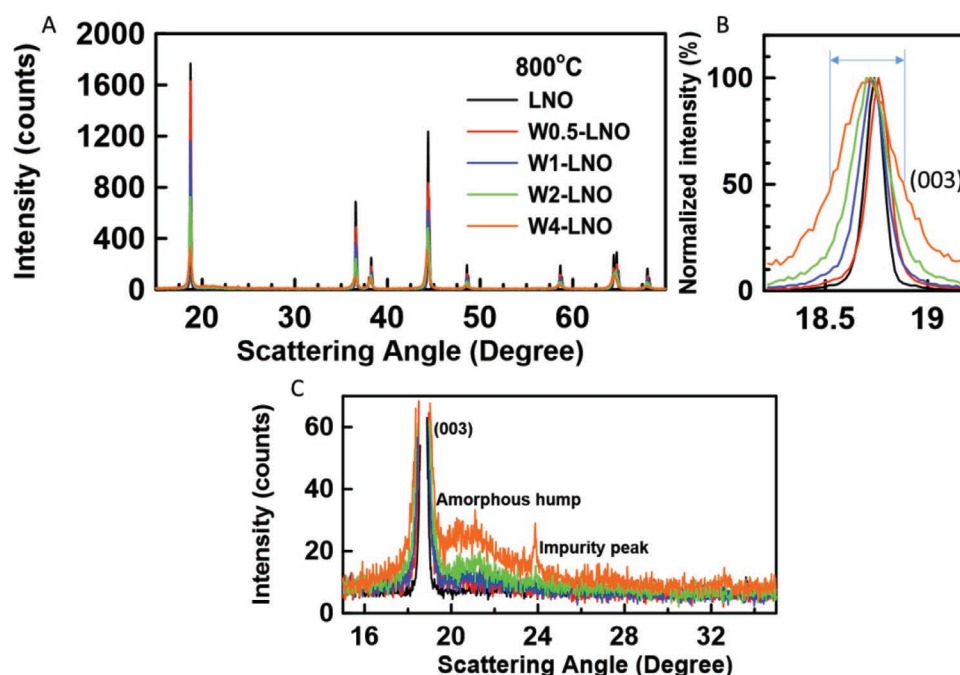


Figure 1. A) XRD patterns of LNO, W0.5-LNO, W1-LNO, W2-LNO, and W4-LNO synthesized at 800°C ; B) Broadening of the peak-height normalized (003) peak; C) Expanded view of the impurity region.

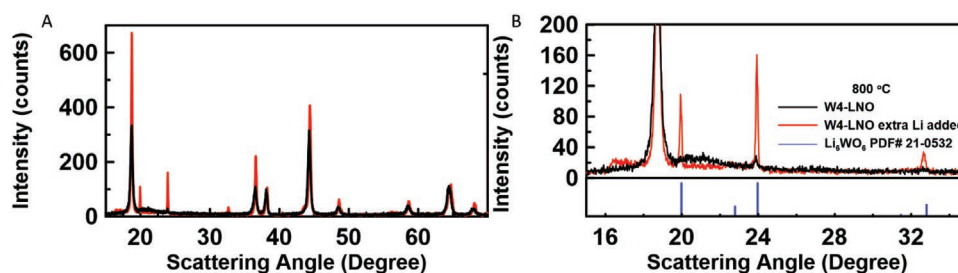


Figure 2. A) XRD patterns of W4-LNO and W4-LNO with extra Li added during synthesis; B) Expanded view of the impurity region.

layered structure as shown in **Figure 2A**. The amorphous hump became less pronounced, and a new phase appeared representing Li_6WO_6 (PDF# 21-0532, **Figure 2B**). The appearance of the Li_6WO_6 phase confirmed that there is a $\text{Li}_x\text{W}_y\text{O}_z$ phase staying outside of layered phase. The Rietveld refinement result is also shown in Table S2 in the Supporting Information. The percentage of Ni in the Li layer decreased to 4.3% when a Li:(Ni+W) ratio of 1.06 was used compared to 8.9% when a Li:(Ni+W) ratio of 1.02 was used. This suggests that the Li_6WO_6 phase consumed a large amount of Li resulting in insufficient Li for stoichiometric LiNiO_2 and causing lithium deficiency as in $\text{Li}_{1-x}\text{Ni}_{1+x}\text{O}_2$. Then some Ni^{3+} transforms to Ni^{2+} to maintain electroneutrality, and some of this Ni^{2+} then moves to the Li layer, thus the percentage of Ni in the Li layer increased. When extra Li was added, to compensate for that lost in the $\text{Li}_x\text{W}_y\text{O}_z$ phase, the Li deficiency in $\text{Li}_{1-x}\text{Ni}_{1+x}\text{O}_2$ decreased.

Figure S1A,B (Supporting Information) shows the W L3-edge X-ray absorption near edge structure (XANES) spectra and Fourier-transformed extended X-ray absorption fine structure (EXAFS) spectra of W1-LNO and a home-made Li_4WO_5 reference. Both the W L3-edge XANES spectra and Fourier-transformed EXAFS spectra of W1-LNO are identical to the spectra of the home-made Li_4WO_5 reference, which implies again that W is incorporated in a $\text{Li}_x\text{W}_y\text{O}_z$ phase. The XRD pattern of home-made Li_4WO_5 in **Figure S1C** (Supporting Information) shows it contains both Li_4WO_5 and Li_6WO_6 . This provides an explanation why the impurity phase in “W4-LNO extra Li added” is Li_6WO_6 (more excess lithium) while the W L3-edge EXAFS spectra of W1-LNO and Li_4WO_5 are identical. The local structures containing the first and second neighbors of W in Li_4WO_5 (**Figure S1D**, Supporting Information) and Li_6WO_6 (**Figure S1E**, Supporting Information) are quite similar, which can explain why the W1-LNO and homemade Li_4WO_5 materials have similar W L3 edge peak positions in XANES and in Fourier-transformed EXAFS spectra.

Figure S2 (Supporting Information) shows the discharge specific capacity versus cycle number for W4-LNO and “W4-LNO extra Li added.” Adding extra Li during heat treatment greatly increased the specific capacity of W4-LNO from 133.5 to 193.9 mAh g^{-1} , further supporting our speculation that the $\text{Li}_x\text{W}_y\text{O}_z$ phase formed and consumes lithium hence causing Li deficiency in $\text{Li}_{1-x}\text{Ni}_{1+x}\text{O}_2$.

In order to clearly determine the location of W in the LNO samples, EELS, performed in a transmission electron microscope (TEM), was carried out on a cross section of the W1-LNO sample. The STEM image of W1-LNO and the EELS mapping of W in **Figure 3A** show that W is mostly concentrated in the grain boundaries between primary particles and on the sur-

face of the secondary particles instead of being incorporated within the grains. Analyzing O-K edge EELS near-edge structure features, it is found that the oxygen K-edge spectrum in the grain boundaries and on the surface of the secondary particles (**Figure S3A**, Supporting Information) does not have a pre-edge while oxygen K-edge spectrum within the grains has a pre-edge feature (**Figure S3B**, Supporting Information). Therefore, it is possible to conclude that the chemical environment/coordination of the oxygen atoms within the grains and the grain boundaries is different. Multiple linear least squares (MLLS) fitting maps with the internal references (using spectra at grain boundaries and spectra within the grains) show that oxygen without a pre-edge are present on all grain boundaries while oxygen with a pre-edge are present inside grains. There is strong correlation between the different near edge structure of the oxygen spectra at the grain boundaries with the maps of W, which infers that the phases having a different oxygen chemical environment are W phases.

In order to determine if the W location would be influenced by the way that W was added, EELS was also carried out on W1-LNO in which W was added by coprecipitation at the precursor synthesis stage (the only sample made by coprecipitation in this work). In the coprecipitated precursor it is possible that W was uniformly distributed inside the precursor, not only on the surface of the precursor when WO_3 was coated by dry particle fusion. EELS mapping of W in **Figure 3B** shows that W was also mostly concentrated in the grain boundaries along with the surface and not significantly distributed into primary particles of W1-LNO where the precursor was made by coprecipitation. This means that even if W was uniformly incorporated throughout the coprecipitated precursor, it is expelled into the grain boundaries during heat treatment with $\text{LiOH} \cdot \text{H}_2\text{O}$.

The scanning electron microscopy (SEM) images in **Figure 4A** shows that the primary particles of LNO were relatively large and that the primary particles become smaller after adding W. ImageJ^[21,22] was used to obtain the average primary particle area, and **Figure 4C** shows the average primary particle radius plotted versus the W-content calculated assuming the primary particle cross sections are circular. **Figure 4C** shows quantitatively the same trend as the images in **Figure 4A**. In order to observe how temperature would influence particle growth, we synthesized LNO and W1-LNO at 700, 750, 800, and 900 °C. SEM images were taken to observe the primary particle growth versus temperature (**Figure 4B**) and ImageJ was used to quantify the primary particle radius of materials synthesized at different temperatures (**Figure 4D**). LNO has relatively large primary particles at 700 °C initially, and the primary particles grow larger with temperature, becoming much larger at 900 °C; while adding W

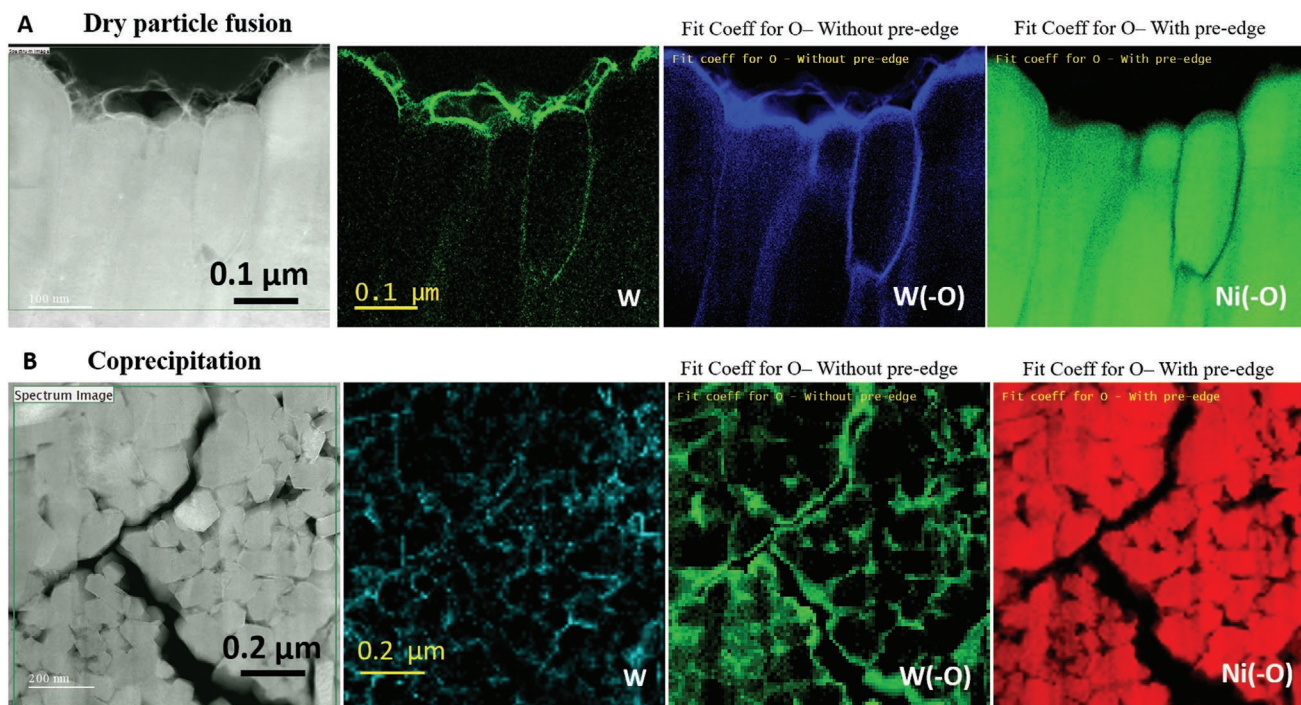


Figure 3. TEM image, EELS mapping of tungsten signal, MLLS fitting of oxygen without pre-edge spectra, MLLS fitting of oxygen with pre-edge spectra of A) W1-LNO sample where the precursor was coated with WO_3 by dry particle fusion and B) W1-LNO sample where the precursor was made by coprecipitation after cycling. The scale bar corresponding to each panel is shown in the left most panel.

effectively suppressed primary particle growth. Primary particles of W1-LNO at 700 °C were small and remained small even though the synthesis temperature increased to 900 °C. SEM images (Figure S4, Supporting Information) at lower magnifications showing morphologies of singular and multiple particles of the above mentioned materials are included in the Supporting Information. In our opinion, the surface nano- WO_3 on $\text{Ni}(\text{OH})_2$ should react with LiOH or Li_2O to form $\text{Li}_x\text{W}_y\text{O}_z$ phases, which normally have melting points in the temperature range of 700–750 °C.^[23] As a result, these $\text{Li}_x\text{W}_y\text{O}_z$ phases can easily wet the surfaces of the secondary grains during synthesis and then infuse along all the grain boundaries between the primary particles. We infer that it is primarily the $\text{Li}_x\text{W}_y\text{O}_z$ phase which wets the surfaces of the primary particle grains that behaves like a barrier to slow down Ni interdiffusion and therefore hinders the growth of the primary grains as temperature increases. Given the lack of detectable W substituting for Ni in LNO, we expect that W within the LNO lattice, if any, would not have a significant effect suppressing grain growth.

Figure 5A shows the discharge specific capacity versus cycle number for samples described above. Adding only 0.5 mol% W greatly improved the specific capacity and capacity retention, and W1-LNO showed the best performance with both best specific capacity and best capacity retention. The peak below 3.6 V shown in the differential capacity curve (dQ/dV) in Figure 5B is normally referred as being in the kinetic hindrance (KH) region^[24] and the peak intensity is very sensitive to the fraction of Ni atoms in the Li layer.^[25] Therefore, the larger KH peak of W0.5-LNO and W1-LNO agrees with the refinements for $\% \text{Ni}_{\text{Li}}$ shown in Table S2 in the Supporting Information. The intensity of the H3→H2 peak^[24] in the dQ/dV versus V curve near 4.2 V

drops with higher W fraction, suggesting the suppression of the H3→H2 phase transition,^[8,24] which agrees with a literature report.^[13] The suppression is caused by the increased fraction of Ni atoms in the Li layer in the samples having more W.^[26,27]

Figure 5C shows the specific capacity versus cycle number of W1-LNO synthesized at 700, 750, 800, and 850 °C. W1-LNO made at 750 and 800 °C have almost overlapping data and behaved better than W1-LNO made at other temperatures. Figure S5 (Supporting Information) shows the XRD patterns of the above-mentioned materials with well-developed layered structure, and the XRD refinement data are included in Table S3 in the Supporting Information. Figure 5D compares the dQ/dV versus V curves of the 2nd, 54th, and the 106th cycle of W1-LNO made at 800 °C. There was a capacity recovery in the KH region and the H3→H2 peak maintained its peak intensity and shape, indicating minimal degradation and good capacity retention of the material.

In a recent paper,^[28] we studied the propensity of various Ni-rich positive electrode materials to resist microcracking under the application of uniaxial pressure. That work showed that the stronger polycrystals can maintain their secondary particle integrity under high stress and avoid microcracking during charge–discharge cycling. Crushing tests applying a pressure from zero up to 500 MPa using an Instron universal testing machine and an appropriate die were performed on LNO synthesized at 800 °C and W1-LNO synthesized at 750 °C. Data collected are shown in Figure S6A in the Supporting Information. The compression work measures the resistance of a material to be crushed which increases from 7.7 J g⁻¹ for LNO to 15.1 J g⁻¹ for W1-LNO, indicating that W1-LNO has greatly increased resistance to fracture. As shown in Figures S6B,C (Supporting

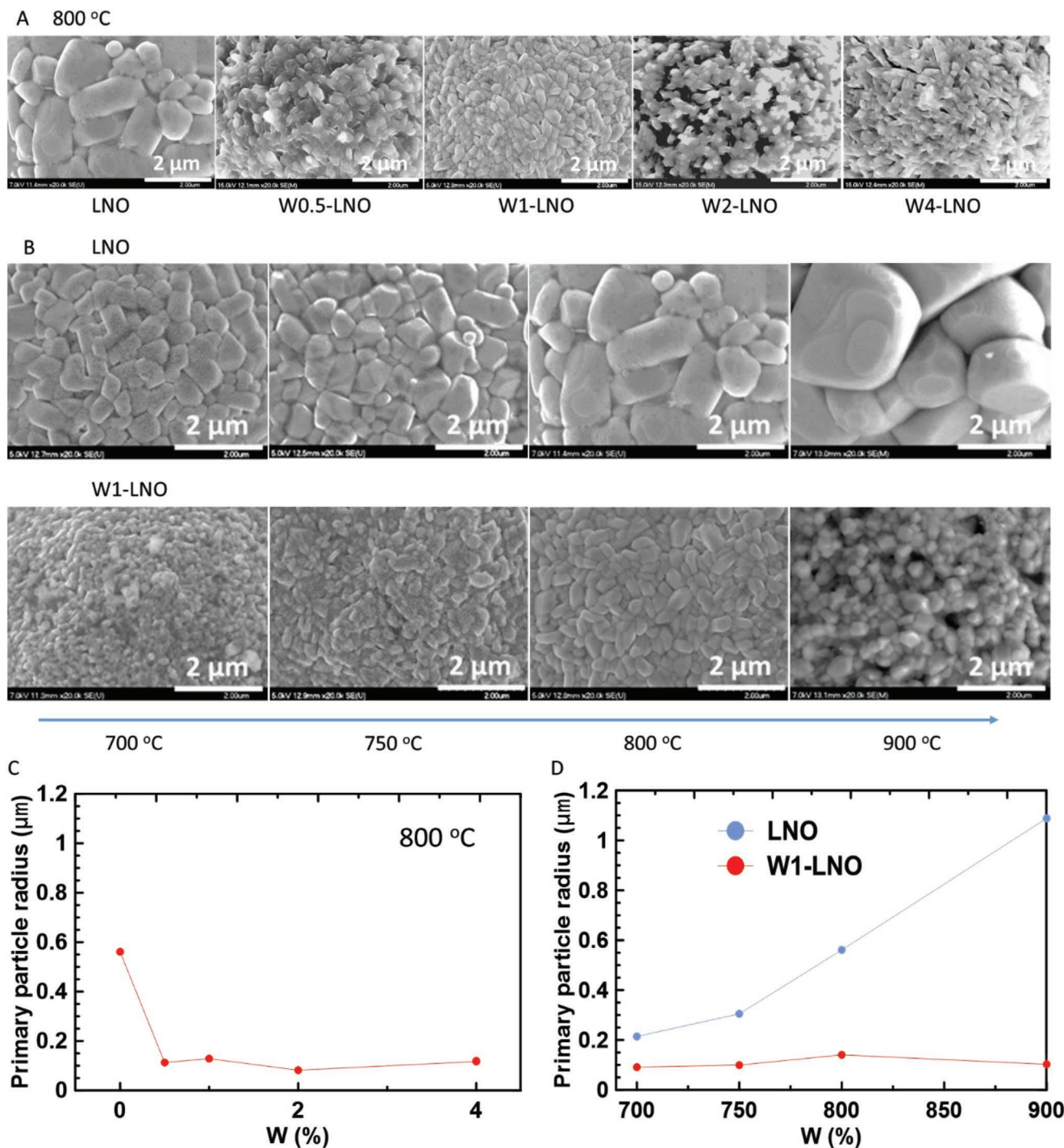


Figure 4. A) SEM images of LNO, W0.5-LNO, W1-LNO, W2-LNO, and W4-LNO synthesized at 800 °C; B) SEM images of LNO and W1-LNO synthesized at 700, 750, 800, and 900 °C; C) average primary particle radii of samples mentioned in (A); D) average primary particle radii of samples mentioned in (B).

Information), LNO heavily fractured after the crushing test to a pressure of 500 MPa, while only a few particles of W1-LNO cracked after crushing, which clearly shows W1-LNO is more resistant to fracture. In our opinion, it is the infusion of the amorphous $\text{Li}_x\text{W}_y\text{O}_z$ phases between the grain boundaries which coats the particle surface, hinders grain growth, improves secondary particle robustness, thus improve material cycling performance.

3. Conclusion

This work clearly shows that W is not incorporated substitutionally for Ni or Li when incorporated as a dopant in LNO. Instead, XRD and EELS have conclusively shown that W is present in amorphous $\text{Li}_x\text{W}_y\text{O}_z$ phases that coat the surfaces of the secondary particles and all the grain boundaries of the primary

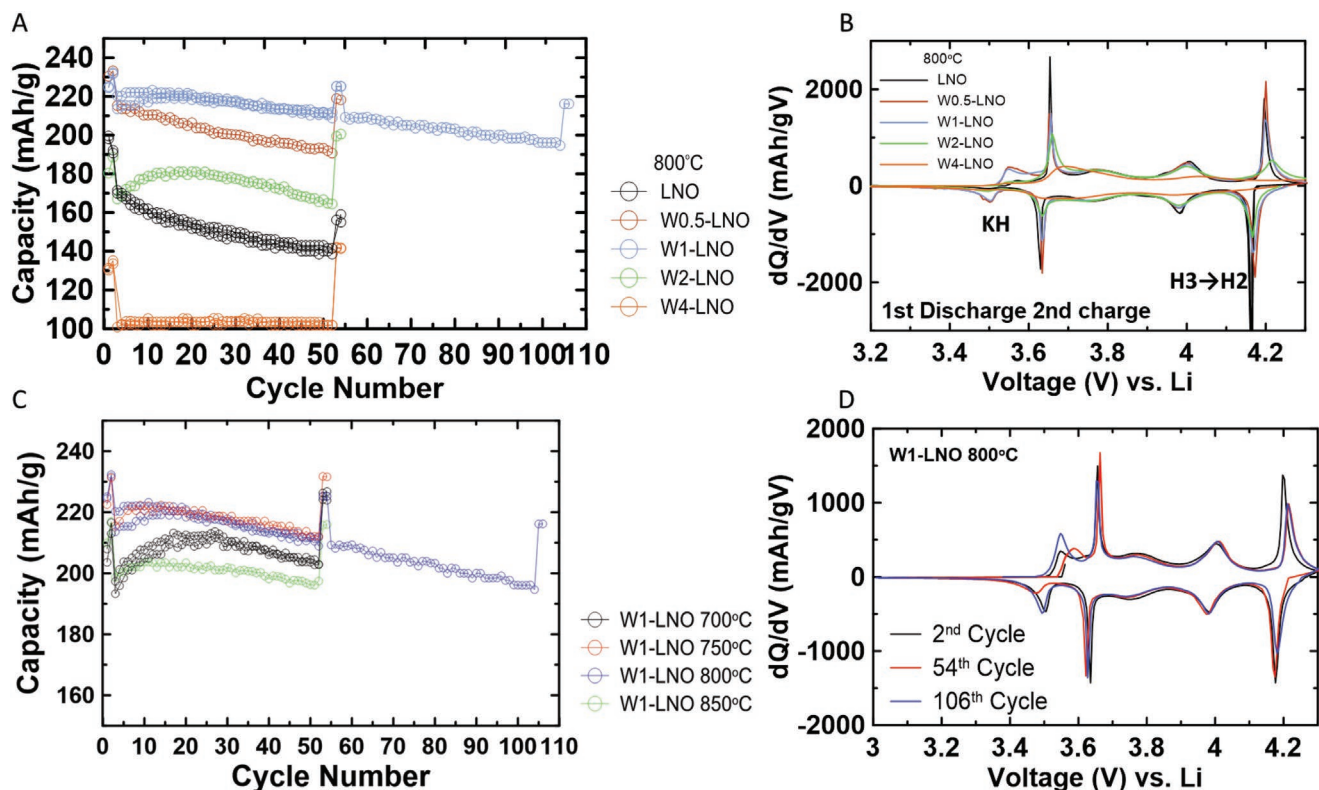


Figure 5. A) Electrochemical cycling performance of LNO, W0.5-LNO, W1-LNO, W2-LNO, and W4-LNO synthesized at 800 °C (2 cycles at C/20, 50 cycles at C/5, and 2 cycles at C/20); B) dQ/dV versus V curves of 1st discharge and 2nd charge process; C) Electrochemical cycling performance of W1-LNO synthesized at 700, 750, 800, and 850 °C; D) Comparison of 2nd cycle and the 54th cycle dQ/dV versus V curves of W1-LNO synthesized at 750 °C.

particles. Given that the WO_3 was only coated on the surfaces of the $Ni(OH)_2$ precursor in the samples made by mechano-fusion, finding W deep within the secondary particles means that the $Li_xW_yO_z$ phases wet the LNO surfaces well. This provides a coating on the primary and secondary particles which may aid in capacity retention. Additionally, the $Li_xW_yO_z$ phases hinder primary particle growth as temperature increases and might appear to act as a “glue” to increase the resistance of the secondary particles to microcracking under applied stress and during charge–discharge cycling.

It is our hope that this paper aid in the understanding and commercialization of Ni-rich positive electrode materials for Li-ion cells.

4. Experimental Section

Precursor Synthesis: A dry particle fusion method described carefully in our previous work^[29,30] was used for this work. Briefly, nanometer-sized Tungsten (VI) oxide (WO_3) powder (<100 nm, from Sigma-Aldrich) was coated on $Ni(OH)_2$ (15 micrometer diameter, from Zoomwe, China) by dry particle fusion to make $(Ni(OH)_2)_{1-x} \cdot (WO_3)_x$ precursors ($x = 0, 0.005, 0.01, 0.02, \text{ and } 0.04$). Material loading weight, spinning speed, and duration are shown in Table S1 in the Supporting Information.

In order to see if the location of W in LNO would be influenced by the way that W was added, the precursor $(Ni(OH)_2)_{0.98} \cdot (NiWO_4)_{0.01}$, which has a $W/(Ni+W)$ molar ratio of 0.01, was made by coprecipitation in a continuously stirred tank reactor (CSTR) (Brunswick Scientific/Eppendorf BioFlo 310) using a method similar to that described by Van Bommel

and Dahn.^[31] 400 mL of 2.0 M $NiSO_4$ and 100 mL of 0.0808 M $NaWO_4$ were prepared separately. A 10.0 M $NaOH(aq)$ solution was used as the source of base for the reaction, while 1 L of 1.0 M $NH_3(aq)$ solution was added into the tank reactor before coprecipitation for metal ion coordination with ammonia to facilitate spherical and dense particle growth during the reaction.^[31] Reagents were added using digital peristaltic pumps (Masterflex L/S 0 7524). $NaOH(aq)$ solution addition was automatically controlled by the pH controller and added as required by a peristaltic pump on the reactor. The vessel was maintained at a temperature of 60 °C and the contents of the reactor were stirred by an overhead stirrer at 1000 rpm. Nitrogen was bubbled (60 sccm (standard cubic centimeter per minute)) into the reactor throughout the reaction to create an inert reaction atmosphere. The reaction proceeded with the addition of 5.0 M $NH_3(aq)$ at 0.14 mL min^{-1} , 400 mL $NiSO_4$ at 0.333 mL min^{-1} , and 100 mL $NaWO_4$ at 0.0833 mL min^{-1} (corresponding to a reaction time of 20 h). After 20 h of reaction time, the hydroxide precursor was rinsed with 4.0 L of water, and then dried at 120 °C overnight.

Cathode Material Synthesis: To synthesize the final products of LNO, W0.5-LNO, W1-LNO, W2-LNO, and W4-LNO, both the precursors prepared by dry particle fusion and by coprecipitation were ground by hand with $LiOH \cdot H_2O$ at a stoichiometric ratio of $Li:(Ni + W) = 1.02:1$. The thoroughly mixed powders were preheated at 480 °C for 3 h under an oxygen flow. After the preheating step, powders were taken out to grind again to ensure excellent mixing. The ground powders were heated at 480 °C for 2 h and 800 °C for another 20 h under oxygen flow at second heating step. In order to get the optimum calcination temperature for W1-LNO, powders were also heated at 700, 750, and 850 °C at the second heating step characterized by charge–discharge cycling in coin cells.

XRD: X-ray diffraction was carried out using a Bruker D8 diffractometer equipped with a Cu-target X-ray source and a diffracted

beam monochromator. Measurements were conducted with a step size of 0.02° and a data collection time of a 3 s per step. The scattering angle (2θ) range was 15° – 70° . A 1 mm divergence slit, 1 mm antiscattering slit, and 0.2 mm receiving slit were used for the measurements. Diffraction patterns were refined using “Rietica.”^[32]

EELS: Electron energy loss spectroscopy (with Gatan Quantum Imaging Filter) was used in a scanning transmission electron microscope (STEM) (double-aberration corrected FEI Titan 80–300) to map the distribution of elements in the samples. The STEM convergence semiangle as well as the EELS collection angle were 19.1 and 55 mrad, respectively. To enhance the signals while reducing beam irradiation effects, the microscope was operated at 200 keV and a direct electron detector (Gatan K2 Summit) was used. Signals were extracted using a simple power law or multiple least-square fitting of reference spectra. Thin samples for EELS and STEM were prepared with a plasma focused ion beam (ThermoFisher Helios G4 PFIB). A two-step process of thin coating of C and W was used to improve the uniformity of the thin areas. It was confirmed, from reference samples that did not contain W, that this two-step process did not generate any residue W on the lamella. The W maps are therefore representative of the W processing steps during the synthesis of the samples.

EXAFS: Extended X-ray absorption fine structure spectroscopy data were collected for the tungsten L3-edge on the IDEAS beamline at the Canadian Light Source. The beamline consists of a bending magnet source with a Ge(220) double-crystal monochromator. Samples were diluted in boron nitride powder and homogenized with a mortar and pestle. Approximately 10 mg of each standard was made up to 200 mg total in boron nitride. For the W-containing LiNiO₂ sample, 50 mg was diluted up to 100 mg total in boron nitride (so that the concentrations of tungsten were relatively similar). All data were collected in fluorescence mode, with the sample oriented 45° to the beam axis. Fluorescence data was collected using a Hitachi Vortex ME4 silicone drift detector with FalconX electronics. The home-made Li₄WO₅ reference sample was synthesized by heating stoichiometric amounts of Li₂CO₃ and WO₃ at 700 °C for 24 h in air.

SEM: A Hitachi S-4700 SEM was used to observe the morphology of the samples. The SEM was operated in secondary electron mode with an accelerating voltage of 15 kV and an emission current of 15 μ A.

Electrochemical Testing: Samples were mixed with Super-S carbon black and polyvinylidene difluoride (PVDF, Kynar 301F, Arkema) in a weight ratio of 92:4:4, and a suitable amount of *N*-methyl-2-pyrrolidone (NMP, 99.5%, Sigma-Aldrich) was added to make a slurry. The slurry was cast on aluminum foil with a 150 μ m notch bar and dried at 120 °C in an oven for 3 h. After drying, the coating was then calendared at a pressure of 2000 atm and then punched into electrodes with a diameter of 12.75 mm. Electrodes were dried at 120 °C under vacuum for 16 h before making coin cells. Coin cells were assembled in an argon-filled glovebox with a negative electrode of Li metal foil, two layers of separator (Celgard #2300) and 1.2 M LiPF₆ (lithium hexafluorophosphate, BASF, 99.9%) in FEC (fluoroethylene carbonate, BASF, 99.94%)/DMC (dimethyl carbonate, Shenzhen Capchem Technology Co., Ltd.) (1:4 v/v) electrolyte. Coin cells were tested using an E-one Moli Energy Canada battery test system at 30 °C. Cells were cycled between 3.0–4.3 V at a current corresponding to C/20 for 2 cycles and then C/5 for 50 cycles and finished with a current of C/20 for 2 cycles.

Crushing Tests: These tests were performed to test the mechanical strength of materials using an Instron universal testing instrument at Dalhousie University. For these tests 0.6 g of material was placed in an appropriate die and pressures from zero to 500 MPa were applied while the displacement of the sample was measured. Readers can refer to ref. [28] for detailed information.

Supporting Information

Supporting Information is available from the Wiley Online Library or from the author.

Acknowledgements

The authors would like to thank NSERC and Tesla Canada for the funding under the auspices of the Industrial Research Chair and Alliance Grant Programs. C.G. thanks the China Scholarship Council for generous support. I.H. and D.R. acknowledge the Killam Predoctoral Scholarship Program for financial support. G.A.B. and N.Z. are grateful to NSERC for supporting their contributions to this work. The STEM-EELS results were obtained at the Canadian Centre for Electron Microscopy, a national facility supported by the Canada Foundation for Innovation under the Major Science Initiative program, NSERC and McMaster University. Part of the work described in this paper was performed at the Canadian Light Source, a national research facility of the University of Saskatchewan, which is supported by the Canada Foundation for Innovation (CFI), NSERC, the National Research Council (NRC), the Canadian Institutes of Health Research (CIHR), the Government of Saskatchewan, and the University of Saskatchewan. The authors would like to acknowledge the support and assistance of David Muir, Beamline Scientist at the IDEAS beamline.

Conflict of Interest

The authors declare no conflict of interest.

Data Availability Statement

The data that support the findings of this study are available from the corresponding author upon reasonable request.

Keywords

lithium nickel oxide, lithium-ion batteries, positive electrode materials, tungsten incorporation

Received: October 1, 2021

Revised: November 27, 2021

Published online:

- [1] M. D. Radin, S. Hy, M. Sina, C. Fang, H. Liu, J. Vinckeviciute, M. Zhang, M. S. Whittingham, Y. S. Meng, A. Van der Ven, *Adv. Energy Mater.* **2017**, *7*, 1602888.
- [2] T. Ohzuku, T. Yanagawa, M. Kouguchi, A. Ueda, *J. Power Sources* **1997**, *68*, 131.
- [3] S. Madhavi, G. V. Subba Rao, B. V. R. Chowdari, S. F. Y. Li, *J. Power Sources* **2001**, *93*, 156.
- [4] Z. Lu, D. D. MacNeil, J. R. Dahn, *Electrochem. Solid-State Lett.* **2001**, *4*, A191.
- [5] M. Yoshio, H. Noguchi, J. ichi Itoh, M. Okada, T. Mouri, *J. Power Sources* **2000**, *90*, 176.
- [6] T. Ohzuku, Y. Makimura, *Chem. Lett.* **2001**, *30*, 642.
- [7] Z. Liu, A. Yu, J. Y. Lee, *J. Power Sources* **1999**, *81–82*, 416.
- [8] H. Li, M. Cormier, N. Zhang, J. Inglis, J. Li, J. R. Dahn, *J. Electrochem. Soc.* **2019**, *166*, A429.
- [9] H. Li, A. Liu, N. Zhang, Y. Wang, S. Yin, H. Wu, J. R. Dahn, *Chem. Mater.* **2019**, *31*, 7574.
- [10] H. Ryu, K. Park, D. R. Yoon, A. Aishova, C. S. Yoon, Y. K. Sun, *Adv. Energy Mater.* **2019**, *9*, 1902698.
- [11] U. H. Kim, D. W. Jun, K. J. Park, Q. Zhang, P. Kaghazchi, D. Aurbach, D. T. Major, G. Goobes, M. Dixit, N. Leifer, C. M. Wang, P. Yan, D. Ahn, K. H. Kim, C. S. Yoon, Y. K. Sun, *Energy Environ. Sci.* **2018**, *11*, 1271.

- [12] W. Li, J. Zhang, Y. Zhou, W. Huang, X. Liu, Z. Li, M. Gao, Z. Chang, N. Li, J. Wang, S. Lu, X. Li, W. Wen, D. Zhu, Y. Lu, W. Zhuang, *ACS Appl. Mater. Interfaces* **2020**, *12*, 47513.
- [13] H. H. Ryu, G. T. Park, C. S. Yoon, Y. K. Sun, *J. Mater. Chem. A* **2019**, *7*, 18580.
- [14] D. Becker, M. Börner, R. Nölle, M. Diehl, S. Klein, U. Rodehorst, R. Schmuck, M. Winter, T. Placke, *ACS Appl. Mater. Interfaces* **2019**, *11*, 18404.
- [15] J. Huang, H. Liu, T. Hu, Y. S. Meng, J. Luo, *J. Power Sources* **2018**, *375*, 21.
- [16] G. K. Williamson, W. H. Hall, *Acta Metall.* **1953**, *1*, 22.
- [17] S. A. Speakman, Basics of X-Ray Powder Diffraction, <http://prism.mit.edu/xray/education/downloads.html> (accessed: December 2021).
- [18] C. Suryanarayana, M. G. Norton, in *X-Ray Diffraction*, Springer **1998**, p. 207.
- [19] R. D. Shannon, *Acta Cryst.* **1976**, *A32*, 751.
- [20] D. Rathore, C. Geng, N. Zaker, I. Hamam, Y. Liu, P. Xiao, G. Botton, J. R. Dahn, C. Yang, *J. Electrochem. Soc.* **2021**, *168*, 120514.
- [21] T. J. Collins, *BioTechniques* **2007**, *43*, S25.
- [22] T. Ferreira, W. Rasband, *ImageJ/Fiji*, <https://imagej.nih.gov/ij/docs/guide/> (accessed: November 2021).
- [23] P. Tabero, A. Frackowiak, *J. Therm. Anal. Calorim.* **2017**, *130*, 311.
- [24] H. Li, N. Zhang, J. Li, J. R. Dahn, *J. Electrochem. Soc.* **2018**, *165*, A2985.
- [25] M. M. Cormier, N. Phattharasupakun, E. Lyle, E. Zsoldos, A. Liu, C. Geng, Y. Liu, H. Li, M. Sawangphruk, J. R. Dahn, *J. Electrochem. Soc.* **2021**, *168*, 090535.
- [26] C. Pouillierie, E. Suard, C. Delmas, *J. Solid State Chem.* **2001**, *158*, 187.
- [27] H. Arai, S. Okada, H. Ohtsuka, M. Ichimura, J. Yamaki, *Solid State Ionics* **1995**, *80*, 261.
- [28] I. Hamam, O. Roeie, D. Rathore, C. Geng, R. Cooke, K. Plucknett, D. P. Bishop, N. Zaker, G. A. Botton, C. Yang, J. R. Dahn, *Cell Rep. Phys. Sci.*, <https://doi.org/10.1016/j.xcrp.2021.100714>.
- [29] C. Geng, S. Trussler, M. Johnson, N. Zaker, B. Scott, G. Botton, J. R. Dahn, *J. Electrochem. Soc.* **2020**, *167*, 110509.
- [30] C. Geng, A. Liu, J. R. Dahn, *Chem. Mater.* **2020**, *32*, 6097.
- [31] A. van Bommel, J. R. Dahn, *Chem. Mater.* **2009**, *21*, 1500.
- [32] R. J. Hill, *American Mineralogist*, **1984**, *69*, 937.